PAPER

Red-emitting fluorescent probes based on sulfur-substituted barbituric acid derivatives: synthesis, properties and biomedical applications†

Xu Feng, [ID] *[a] Jianfei Jin,[b] Yun Si,[b] Huanmin Zhang[b] and Chenxi Luo[b]

Fluorescence bioimaging has emerged as a vital tool for tracking dynamic biochemical processes and monitoring disease biomarkers *in vivo*. This technique has demonstrated significant clinical and commercial potential in fluorescence-guided surgery (FGS) for tumor treatment, attributed to its real-time visualization capabilities and high biocompatibility. To achieve precise delineation of tumor boundaries and complete tumor resection, the rational design and selection of contrast agents are critical. Herein, we report a novel red-emitting fluorophore, TTS, based on thiobarbituric acid (TBA) derivatives and tetraphenylethylene. The design strategy, synthetic route, optical properties, and cytotoxicity of TTS are systematically described. Benefiting from its highly twisted molecular conformation and enhanced intramolecular charge transfer (ICT) effect, TTS exhibits superior aggregation-induced emission (AIE) characteristics with emission wavelengths extending into the NIR-I region (700−900 nm), as well as a reactive oxygen species (ROS)-generating capability. Systematic *in vivo* evaluations further demonstrate that TTS nanoparticles (NPs), which were formulated with DSPE-PEG2000 encapsulation, can accurately illuminate osteosarcoma tissues and effectively guide surgical resection through the enhanced permeability and retention (EPR) effect. This novel fluorophore not only boosts the development of AIE-based medical materials but also benefits intraoperative fluorescence imaging for clinical applications.

Introduction

Osteosarcoma (OS), a high-grade malignant tumor originating from mesenchymal tissues (composed of spindle-shaped stromal cells capable of producing osteoid), is the most common primary malignant bone tumor in adolescent patients.[1,2] It predominantly arises in bones with a rapid growth rate.[3] Current clinical management relies on surgical resection combined with radiotherapy and chemotherapy, achieving a 5-year survival rate of 60–66% in non-metastatic cases; however, this rate drops to 20–30% for patients with metastatic disease.[4] Complete tumor resection is therefore critical to mitigate metastatic risks and improve prognosis. In recent years, fluorescence-guided surgery (FGS) has emerged as a promising therapeutic method for tumor management. Compared to other techniques, FGS offers lower equipment complexity, prolonged imaging duration, and real-time visualization of pathological margins, thereby enhancing tumor clearance rates while minimizing residual lesions and postoperative complications.[5–9]

[a]Department of Orthopaedics, Yiwu Central Hospital, 699 Jiangdong Middle Road, Yiwu, Zhejiang Province, 322000, PR China. E-mail: 19905898620@163.com

[b]Zhejiang Yike Biotech. Co., Ltd, Yiwu, Zhejiang Province, China

† Electronic supplementary information (ESI) available. See DOI: https://doi.org/10.1039/d5ra02821c
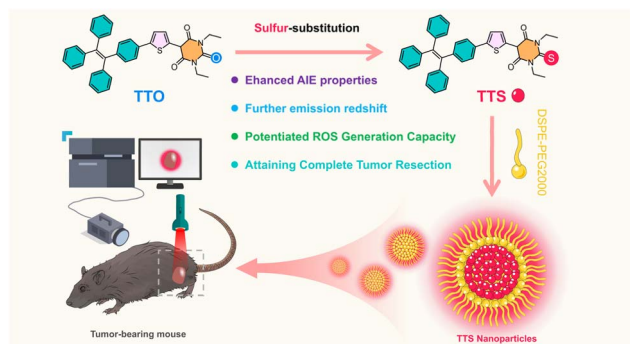
Despite its extensive investigation in other tumors, the application of FGS in osteosarcoma treatment remains underexplored. On the other hand, a key limitation of conventional fluoroprobes lies in aggregation-caused quenching (ACQ), where strong intermolecular π–π stacking in aggregated states drastically reduces fluorescence intensity, compromising imaging resolution in internal environments. To circumvent this limitation, the concept of AIE has emerged as a paradigm-shifting strategy since 2001. Unlike conventional ACQ dyes, AIE luminogens (AIEgens) exhibit weak fluorescence in dilute solutions but significantly enhanced emission in aggregated or solid states.[10–13] This property endows AIEgens with superior fluorescence efficiency and photostability, substantially improving imaging contrast in FGS according to previous literature.[14–17] For example, Chen and co-workers synthesized a pair of geometric isomers exhibiting typical AIE properties, named as ZZ-HPB-NC and EE-HPB-NC. In their study, these two molecules were successfully used in fluorescence navigation for liver tumor resection in mice and accurately locate liver lesions during surgery.[18] In this study, we innovatively employed sulfur-substituted TBA as an electron acceptor and a classic AIEgen, tetraphenylethylene (TPE), as an electron donor to construct a Donor−π−acceptor (D−π−A) conjugated system through thiophene bridging (Scheme 1). This approach successfully yielded a novel AIE molecule, TTS, enjoying convenient synthesis, AIE

Scheme 1 Schematic illustration of TTO/TTS structures and *in vivo* imaging in mouse models.

Scheme 2 Synthetic routes to TTO and TTS.

characteristics, red-emitting emission and ROS-generating capability. In the subsequent *in vivo* experimental evaluation, TTS-encapsulated NPs efficiently penetrated and accumulated in osteosarcoma tissues *via* the EPR effect, enabling precise tumor visualization and significantly enhancing surgical resection accuracy. This work confirmed the substantial clinical translational potential of AIEgens-mediated intraoperative fluorescence imaging in osteosarcoma surgery, benefiting both precision medicine and translational medicine.

Results and discussion

Design and synthesis

Among strategies to extend the emission wavelength of fluorescent molecules, constructing donor–acceptor (D–A) structures with a strengthened push–pull electronic effect to enhance ICT effort has been widely adopted. In this study, we designed a molecular system based on the D–A framework, selecting 1,3-diethylbarbituric acid as the electron-accepting unit and TPE, a classic AIEgen, as the electron-donating unit and molecular rotor to induce AIE characteristics. To further extend the molecular conjugation length, we introduced thiophene into the D–A system as the π-bridge to construct a "D–π–A" conjugated backbone, yielding the target molecule TTO. Based on previous reports,[19] we replaced the oxygen atom in the acceptor unit of TTO with a Group *via* sulfur atom to investigate non-metallic heavy atom effect on the optical properties of AIEgens, thereby synthesizing another target molecule TTS. The detailed synthetic routes of the target compounds are illustrated in Scheme 2. First, 1,3-diethylbarbituric acid was synthesized *via* condensation of malonic acid with 1,3-diethylurea; similarly, 1,3-diethylthiobarbituric acid was prepared by condensation of dimethyl malonate with 1,3-diethylthiourea. Subsequently, 1-(4-bromophenyl)-1,2,2-triphenylethene was converted to 1-(4-(pinacol phenylboronate))-1,2,2-triphenylethene *via* a Suzuki–Miyaura coupling reaction, followed by a Suzuki coupling with 5-bromothiophene-2-carbaldehyde catalyzed by tetrakis(triphenylphosphine)palladium (0), yielding the intermediate 5-(4-(1,2,2-triphenylvinyl)phenyl)thiophene-2-carbaldehyde. Finally, dehydration–condensation reactions between the intermediate and either 1,3-diethylbarbituric acid or 1,3-diethylthiobarbituric

acid afforded the target products TTO and TTS, respectively. The structures of the target compounds were confirmed by nuclear magnetic resonance (NMR) spectroscopy and high-resolution mass spectrometry (HRMS) (Fig. S1–S9†).

Optical properties

The optical properties of TTO and TTS were then investigated. As shown in Fig. S10A,† compound TTO exhibited maximum absorption wavelengths at 453 nm in toluene (Tol), dichloromethane (DCM), tetrahydrofuran (THF), and dimethyl sulfoxide (DMSO), whereas compound TTS displayed red-shifted absorption peaks at 479 nm under identical solvent conditions (Fig. 1A). Correspondingly, the emission peaks of TTS in
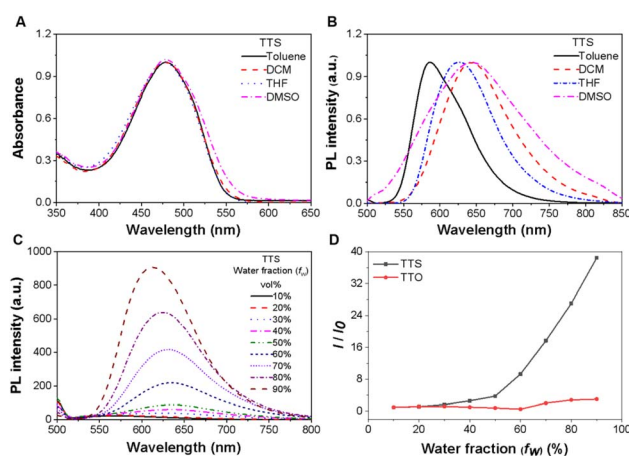

Fig. 1 (A) UV-vis absorption spectra of TTS in various organic solvents. (B) Fluorescence emission spectra of TTS in various organic solvents. (C) Normalized fluorescence emission spectra of TTS *versus* water fraction (f_w) in water/tetrahydrofuran (THF) mixtures. (D) Plot of PL peak intensities of TTO and TTS *versus* water fraction (f_w) in water/THF mixtures. I_0 and I represent the PL intensities of the compounds in water/THF mixtures with $f_w = 10\%$ and $f_w > 10\%$, respectively.

Table 1 Absolute quantum yields of TTO/TTS in solution, aggregative and solid state

Compound	Solution[a] (%)	Aggregation[b] (%)	Solid[c] (%)	λ_{ex} (nm)
TTO	1.08	3.32	3.51	450
TTS	2.23	8.56	9.22	475

[a] Measured in THF with 10 μM TTO or TTS. [b] Measured in water/THF mixtures (f_w = 90%) with 10 μM TTO or TTS. [c] Tested in powder state.

these solvents showed a red shift of approximately 13 nm compared to TTO (Fig. 1B and S10B†).

We also investigated the AIE characteristics of two fluorescent probes in THF/water mixed solvents at different water contents (f_w) (Fig. 1C and D). For TTS, the fluorescence intensity showed a progressive 38-fold enhancement with increasing f_w from 0% to 90%, indicating excellent AIE characteristics. In contrast, the TTO system exhibited dual-phase fluorescence responses: emission wavelength displayed a redshift with concomitant fluorescence quenching as f_w increased from 0% to 60%, which was predominantly attributed to solvent polarity-mediated twisted intramolecular charge transfer (TICT) effects; when f_w exceeded 60%, the fluorescence intensity gradually recovered but only reached threefold the initial value (Fig. S11†). In addition, the absolute quantum yields presented in Table 1 demonstrate that TTS exhibits higher values than TTO in both aggregated and solid states, which further confirm its superior AIE characteristics.

As an emerging therapy for cancer treatment, photodynamic therapy (PDT) uses photosensitizers that, after being excited by light at a specific wavelength, react with the molecular oxygen to create reactive oxygen species (ROS) in the target tissue, resulting in cell death.[20,21] Therefore, ROS generation capability constitutes a critical determinant of PDT efficacy. We also investigated the ROS generation of TTO and TTS for their potential in PDT. The ROS generation capability under broad-spectrum irradiation (380–780 nm, 50 mW cm^{-2}) was

assessed using 2′,7′-dichlorodihydrofluorescein diacetate (DCF-DA). As shown in Fig. 2, exposure of DCF-DA (5 μM) to 10 μM TTO and TTS with or without tris(4-bromophenyl)amine (TBPA) which acted as a singlet oxygen scavenger under irradiation,[22] respectively. As a result, TTS displayed a stronger time-dependent enhancement of 2′,7′-dichlorofluorescein (DCF) fluorescence intensity (λ_{em} = 524 nm) compared to TTO during 300 s irradiation. Notably, the fluorescence enhancement of DCF treated with TTO or TTS are completely suppressed upon addition of TBPA, confirming singlet oxygen as the dominant ROS species generated. In addition, as a reference photosensitizer with efficient singlet oxygen generation, methylene blue exhibited a 7.06-fold enhancement in DCF fluorescence intensity, while TTO showed 1.76-fold enhancement and TTS exhibited 4.06-fold enhancement under identical experimental conditions. Although methylene blue presents better performance, the singlet oxygen production capability of TTO and TTS are still comparable to that of methylene blue. These results establish TTS as a promising photosensitizer for PDT in tumor treatment.

To further decipher the photochemical and photophysical properties mentioned above, we performed density functional theory (DFT) and time-dependent density functional theory (TD-DFT) investigations using B3LYP, CAM-B3LYP, PBE0 and ωB97XD functionals to analyze the excited-state electronic structures of TTO and TTS (Fig S12–S14†). The results from these calculations support the same mechanistic conclusions. As shown in Fig. 3A and Table S1,† with the ωB97XD functional, electrons of the TTO fluorescent probe are delocalized over the entire molecule in the highest occupied molecular orbital (HOMO), while the excited electrons are mainly localized within the thiophene and barbituric acid conjugate system in the lowest unoccupied molecular orbital (LUMO), resulting in a HOMO–LUMO energy gap (ΔE) of 6.438 eV. This HOMO-to-LUMO transition demonstrates evident ICT characteristic. In
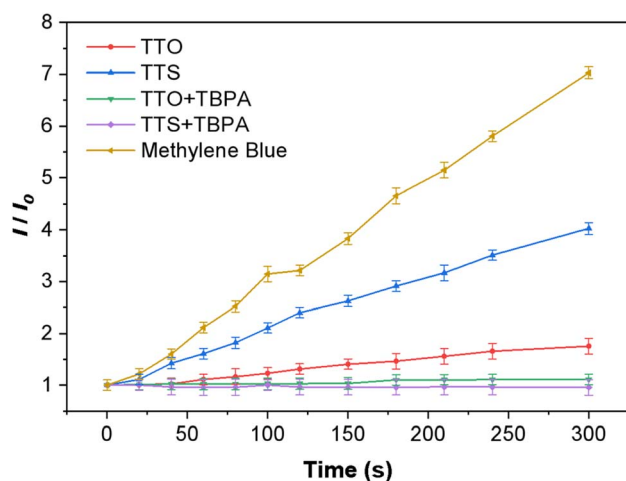

Fig. 2 Fluorescence intensity enhancement of DCF at 524 nm *versus* light irradiation time of TTO, TTS, TTO + TBPA, TTS + TBPA and methylene blue.
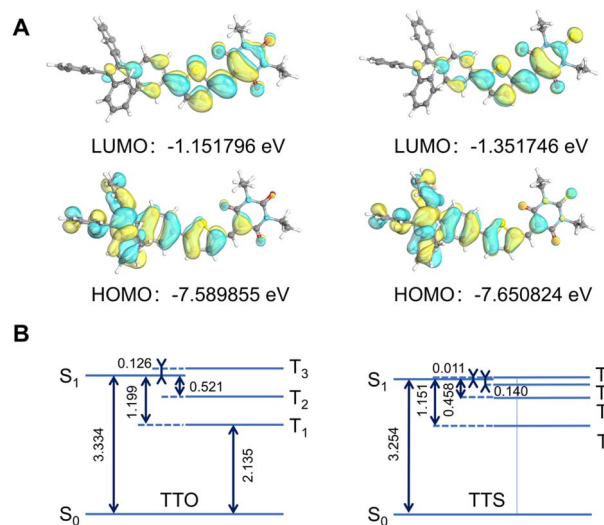

Fig. 3 (A) HOMO−LUMO plots of TTO and TTS calculated by the DFT/ωB97XD/def2-TZVP. (B) Energy diagrams of TTO and TTS as calculated using TD-DFT.

contrast, the sulfur-substituted TTS probe exhibits a reduced ΔE (6.299 eV). The narrowed energy bandgap results in red-shifted light absorption band of TTS. Moreover, as shown in Fig. 3B, the calculated energy gap (0.150 eV) between the lowest singlet (ES1) and involved triplet (ET3) excited states of TTS are considerably smaller than the calculated energy gap (0.521 eV) between the lowest singlet (ES1) and involved triplet (ET2) excited states of TTO, which facilitates the singlet-triplet inter-system crossing (ISC) processes. Consequently, the highly reactive and long-lasting triplet excited states of TTS are more readily obtained and can further electron transferred to oxygen (type I) or/and energy transferred to a ground state triplet oxygen (type II) to produce ROS.[23] In conclusion, these calculation results are consistent with better ICT characteristics and ROS generation capability of TTS. Notably, the HOMO energy levels of TTO and TTS are −5.593 eV and −5.641 eV, respectively, revealing that TTO exhibits better conjugation compared to TTS. Based on this, we speculate that the distinct AIE behavior between TTS and TTO arises from two factors: (i) TTO's extended conjugation probably promotes planar molecular backbones to form intermolecular interactions via $n-\pi^*$ stacking,[24] thereby reducing fluorescence intensity in aggregated states; (ii) the incorporation of sulfur atoms with larger atomic radius could induce additional steric hindrance in TTS's molecular skeleton, suppressing intermolecular $\pi-\pi$ overlap in aggregates and consequently enhancing its AIE performance.[25,26]

Biomedical application

Since TTO and TTS demonstrate neither water solubility nor fluorescence emission in their non-aggregated states, they are unsuitable for direct application in biomedical experiments. Therefore, as shown in Fig. S15 and S16,† we employed 1,2-distearoyl-sn-glycero-3-phosphoethanolamine-polyethylene glycol 2000 (DSPE-PEG2000) as the carrier material to prepare nanoparticle suspensions of TTS and TTO, achieving encapsulation efficiencies of 81.1% and 80.6%, respectively. As shown in Fig. 4A and B, the hydrodynamic diameters of TTO NPs and TTS NPs were determined by dynamic light scattering (DLS) and further confirmed by transmission electron microscopy (TEM). All NPs exhibited uniform near-spherical morphology with an average diameter of approximately 100 mm, indicating the successful construction of a monodisperse colloidal system. Fluorescence spectral analysis (Fig. 4C and D) revealed that TTO NPs displayed a maximum absorption wavelength at 450 nm and an emission peak at 605 nm, while TTS NPs exhibited a red-shifted absorption wavelength to 475 nm with a corresponding emission peak red-shifted to 638 nm. Both TTO and TTS demonstrated significant Stokes shifts ($\Delta\lambda > 150$ nm), which effectively reduce Rayleigh scattering and self-absorption interference from the fluorophores themselves, thereby substantially enhancing the imaging signal-to-noise ratio.

As a prerequisite for conducting biomedical experiments, the cytotoxicity of TTO NPs and TTS NPs toward normal somatic cells were evaluated using the 3-(4,5-dimethylthiazol-2-yl)-2,5-diphenyltetrazolium bromide (MTT) assay on murine smooth
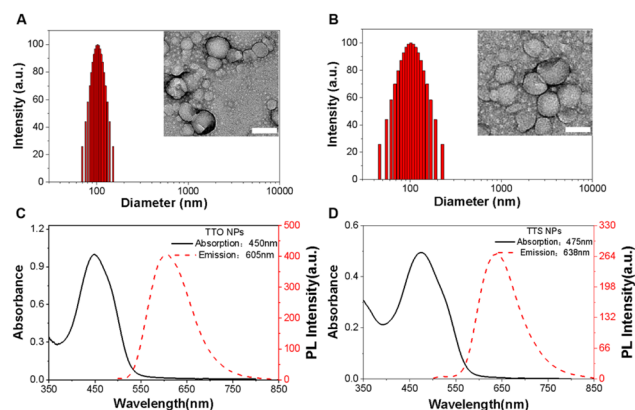

Fig. 4 (A) Dynamic light scattering (DLS) diameter of TTO NPs; inset: transmission electron microscopy (TEM) image of the NPs. (B) DLS diameter of TTS NPs; inset: TEM image of the NPs. (C) UV-vis absorption and fluorescence emission spectra of TTO NPs. (D) UV-vis absorption and fluorescence emission spectra of TTS NPs.

muscle cells (SMCs). As shown in Fig. S18,† after 24 hours of incubation with TTO nanoparticles under light irradiation, the cell viability of SMCs gradually declined, yet consistently remained above 90% as nanoparticle concentrations increased from 10 to 50 μM. In contrast, incubation with TTS nanoparticles under identical conditions resulted in a more pronounced reduction in SMC viability, declining to 81% as nanoparticle concentrations increased from 10 to 50 μM. These results match with the stronger singlet oxygen production capability of TTS compared to that of TTO and indicate that both NPs exhibited excellent biocompatibility. The cytotoxicity evaluations of TTO NPs and TTS NPs toward SMCs in the dark were also performed (Fig. S17†). To evaluate in vivo tumor imaging performance of TTO NPs and TTS NPs, a series of experiments were conducted in C3H mouse models bearing LM8 osteosarcoma subcutaneous tumors. The tumor-bearing mice were intravenously administered via the tail vein with 160 μmol L^{-1} suspensions of TTO NPs or TTS NPs, followed by whole-body fluorescence imaging using the IVIS Spectrum system. As shown in Fig. 5, both NPs demonstrated specific accumulation at the tumor 12 hours post-injection, with fluorescence signals closely corresponding to the actual tumor
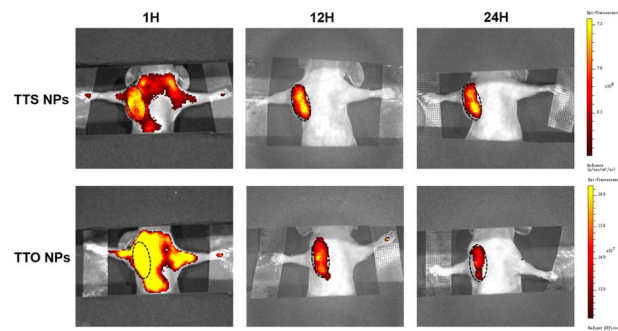

Fig. 5 Fluorescence imaging and average radiance of TTO and TTS in the LM8 osteosarcoma subcutaneous tumors model at different time points. The area of radiance sampling is denoted by black circles.
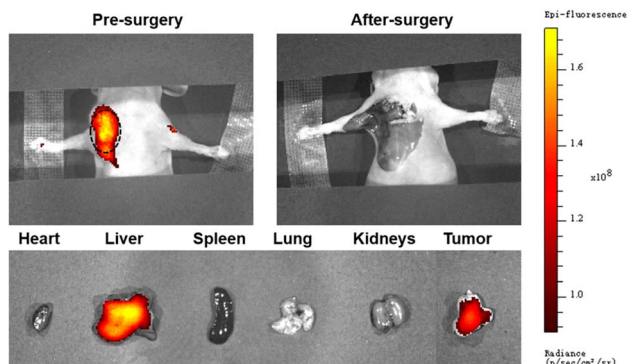
Fig. 6 Preoperative and postoperative fluorescence images of the mouse bearing LM8 osteosarcoma subcutaneous tumors 12 hours after administering 160 μmol L^{-1} of TTO and *ex vivo* fluorescence images of the same mouse. The actual position of tumor is denoted by a black circle.

contours. Notably, TTS NPs exhibited dramatically higher fluorescence intensity than TTO NPs and maintained precise delineation of tumor boundaries even at 24 hours post-injection, whereas the fluorescence signal of TTO NPs significantly diminished and partially dissipated within tumor regions. It is supposed that TTS NPs achieved enhanced tumor enrichment and retention *via* the EPR effect within the tumor microenvironment, while their superior AIE properties resulted in markedly improved fluorescence intensity and prolonged signal duration (>24 h) compared to TTO NPs.

To further compare their performance on FGS, fluorescence-guided tumor resection was performed on two additional groups of LM8 osteosarcoma-bearing C3H mice 12 hours after fluorescent probe injection. Pre-operative and post-operative whole-body imaging, as well as *ex vivo* tissue biodistribution imaging, were performed using IVIS systems (Fig. 6 and 7). The results revealed that both TTO NPs and TTS NPs selectively accumulated in tumor tissues, with negligible fluorescence signals detected in other major organs excluding the liver, confirming hepatic metabolism as the primary elimination

pathway. Notably, TTS NPs demonstrated significantly stronger tumor fluorescence intensity and less hepatic accumulation compared to TTO NPs. Post-operative whole-body IVIS imaging showed no residual tumor fluorescence signals, validating complete resection of light-up tumors. Collectively, the superior optical properties of TTS underscore its potential as an effective intraoperative contrast agent for osteosarcoma resection.

Conclusions

In this study, we developed a novel class of AIE-active bioprobes based on cost-effective and readily available barbituric acid. Through molecular engineering strategies, we first constructed a D–π–A structured AIE fluorophore TTO with tetraphenylethylene as the electron donor, thiophene as the π-bridge and barbituric acid as the electron acceptor. The distorted molecular backbone endowed intrinsic AIE properties, while the extended conjugation facilitated fluorescence emission redshift. *Via* an innovative heavy-atom substitution strategy by replacing oxygen atoms with sulfur atoms, we synthesized a thio-substituted derivative TTS exhibiting a reduced electronic bandgap ($\Delta E = 2.66$ eV) and the following unique properties: (i) a substantially improved AIE performance, achieving over 38-fold brightness amplification in the aggregated state; (ii) a further emission redshift of 13 nm, extending coverage into the NIR region and (iii) a ROS-generating capability which is essential for PDT. To explore its clinical translational potential, TTS was encapsulated with DSPE-PEG2000 to form NPs, which were evaluated for fluorescence-guided resection of subcutaneous LM8 osteosarcoma tumor models in C3H mice. Imaging results confirmed that TTS efficiently accumulated and exhibited long-term retention of more than 24 hours in tumor tissues through the EPR effect within the tumor microenvironment, thereby enabling precise surgical excision. These findings not only validate the feasibility of heavy-atom substitution for fine-tuning AIE molecular properties but also provide a solid foundation for the clinical application of AIE fluorophores in osteosarcoma and other malignant tumor resection surgeries.

Fig. 7 Preoperative and postoperative fluorescence images of the mouse bearing LM8 osteosarcoma subcutaneous tumors 12 hours after administering 160 μmol L^{-1} of TTS and *ex vivo* fluorescence images of the same mouse. The actual position of tumor is denoted by a black circle.

Experimental

Materials

Malonic acid, dimethyl malonate, *N,N*′-diethylthiourea, 1,3-diethylurea, 1-(4-bromophenyl)-1,2,2-triphenylethylene, 4,4,4′,4′,5,5,5′,5′-octamethyl-2,2′-bi(1,3,2-dioxaborolane), and 5-bromothiophene-2-carbaldehyde were purchased from Bide Pharmatech Co., Ltd (Shanghai, China). 1,1′-Bis(diphenylphosphino)ferrocene palladium dichloride and tetrakis(triphenylphosphine)palladium were obtained from J&K Scientific (Beijing, China). All other chemicals and solvents were procured from commercial suppliers and used without further purification unless otherwise specified.

General methods

Moisture-sensitive and oxygen-sensitive reactions were performed in an inert nitrogen atmosphere. UV-vis absorption
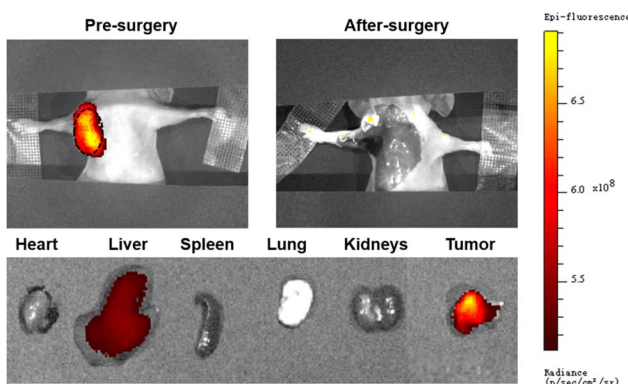
spectra were acquired using a Shimadzu UV-1900i spectrophotometer, scanning across a wavelength range of 440–900 nm. Fluorescence spectra were measured with a Shimadzu RF-6000 fluorescence spectrometer, with the excitation wavelength fixed at the analyte's maximum absorption wavelength and emission spectra collected from 500 to 900 nm. The molecular structures of fluorescent compounds were elucidated *via* liquid-state nuclear magnetic resonance (NMR) spectroscopy (BR1). High-resolution mass spectra (HRMS) were measured on an Agilent LC-QTOF-MS mass spectrometry. Nanoparticle characterization was conducted through dynamic light scattering (DLS) and transmission electron microscopy (TEM). Absolute quantum yields were measured on an Edinburgh FS5 spectrofluorometer.

Synthetic procedures

Synthesis of compound 1. A mixture of malonic acid (208 mg, 2 mmol) and 1,3-diethylurea (232 mg, 2 mmol) was dissolved in acetic acid (2 mL). The mixture was heated to 60 °C, followed by the addition of acetic anhydride (2 mL). The reaction was allowed to proceed for 6 h at this temperature. Subsequently, ultra-pure water (1 mL) was added, and the mixture was heated to 70 °C for an additional 0.5 h. After completion of the reaction, the organic phase was extracted with ethyl acetate (3 × 10 mL). The combined organic layers were concentrated under reduced pressure to afford the crude product. The crude product was purified by column chromatography (hexane/ethyl acetate) to give compound 1 with a 97% yield. ^{1}H NMR (400 MHz, CDCl$_3$): δ 3.95 (q, $J = 7.1$ Hz, 4H), 3.65 (s, 2H), 1.22 (t, $J = 7.1$ Hz, 1H).

Synthesis of compound 2. In the reaction mixture of diethylmalonate (0.19 g, 1.2 mmol) and 1, 3-diethylthiourea (0.13 g, 1.0 mmol), sodium ethoxide (0.06 g, 1.0 mmol) was added. The above resulting reaction mixture was refluxed for 8 h and white precipitates were appeared. The resulting reaction mixture was diluted with 15 mL hot water and hydrochloric acid was added to make the solution acidic. The clear solution was filtered and cooled for overnight. The resulting white precipitates were filtered. The obtained precipitates were washed with cold water, dried and further purified by column chromatography with hexane: Ethyl acetate to give compound 2 with a 96% yield. ^{1}H NMR (400 MHz, CDCl$_3$) δ 4.55 (dq, $J = 12.0, 7.0$ Hz, 1H), 2.74 (s, 0H), 1.30 (dt, $J = 10.4, 7.0$ Hz, 1H).

Synthesis of compound TTO. Compound 3 and compound 4 were synthesized according to the previous literature.[27,28] A mixture of compound 1 (226 mg, 0.6 mmol) and compound 4 (120 mg, 0.66 mmol) was dissolved in acetonitrile (6 mL). Then 2 drops of piperidine were added, and the reaction was 8 h at reflux temperature under nitrogen atmosphere. The reaction is cooled to room temperature, filtered, and washed to produce a red solid TTO with a 95% yield. ^{1}H NMR (400 MHz, CDCl$_3$) δ 8.64 (s, 1H), 7.82 (d, $J = 4.2$ Hz, 1H), 7.54 (d, $J = 8.4$ Hz, 2H), 7.44 (d, $J = 4.2$ Hz, 1H), 7.16–7.10 (m, 10H), 7.08–7.03 (m, 7H), 4.11–4.03 (m, 4H), 1.32–1.24 (m, 6H). ^{13}C NMR (101 MHz, CDCl$_3$) δ 162.45, 161.63, 160.22, 150.61, 148.46, 146.76, 145.81, 143.43, 143.25, 142.21, 140.02, 136.13, 132.20, 131.43, 131.34, 131.10, 127.96, 127.89, 127.74, 126.93, 126.78, 126.73, 126.06,

124.36, 109.76, 37.49, 36.73, 13.50, 13.41. HRMS, m/z calcd for C$_{39}$H$_{32}$N$_2$O$_3$S: 608.2134; found 609.2203 (M + H)$^+$.

Synthesis of compound TTS. Compound 2 (200 mg, 0.46 mmol) and compound 4 (100 mg, 0.5 mmol) were dissolved in acetonitrile (6 mL). Then 2 drops of piperidine were added, and the reaction was 8 h at reflux temperature under nitrogen atmosphere. The reaction is cooled to room temperature, filtered, and washed to produce a red solid TTO with a 95% yield. ^{1}H NMR (400 MHz, CDCl$_3$) δ 8.30 (d, $J = 15.2$ Hz, 1H), 8.11 (d, $J = 15.2$ Hz, 1H), 7.41–7.36 (m, 3H), 7.27 (s, 1H), 7.14–7.09 (m, 9H), 7.08–7.00 (m, 7H), 4.60–4.51 (m, 4H), 1.31 (tt, $J = 8.0, 4.0$ Hz, 6H). ^{13}C NMR (101 MHz, CDCl$_3$) δ 182.95, 176.13, 166.81, 157.99, 149.82, 143.79, 142.45, 142.29, 140.91, 139.04, 138.74, 138.61, 134.09, 131.08, 130.37, 130.29, 126.87, 126.79, 126.66, 125.77, 125.66, 125.60, 124.29, 123.45, 117.76, 42.45, 42.09, 13.09. HRMS, m/z calcd for C$_{39}$H$_{32}$N$_2$O$_2$S$_2$: 624.1905; found 625.1977 (M + H)$^+$.

Preparation of nanoparticles. 1 mg of lipid-soluble TTO or TTS and 2 mg of amphiphilic polymer DSPE-PEG2000 (1,2-distearoyl-*sn*-glycero-3-phosphoethanolamine-*N*-[methoxy(polyethylene glycol)-2000]) were dissolved in 1.0 mL of tetrahydrofuran (THF). The mixture was rapidly injected into 10 mL of ultrapure water under ultrasonic irradiation for 10 minutes. The residual THF was removed by nitrogen purging, and the product was stored at 4 °C for future use. The concentration of the prepared NPs was 160 μmol mL^{-1}. The encapsulation efficiencies of TTO and TTS into the nanoparticles were quantified as follows: first, the initial concentration of the encapsulated agents in the solution was defined as C_i. Following nanoparticles preparation, the nanoparticle suspension was dialyzed for 24 h. Subsequently, 100 μL of the dialyzed suspension was mixed with 900 μL of THF to dissolve the Nanoparticles and release the encapsulated agents. As shown in Fig S12 and S13,† concentration of agents (C_e) was determined by measuring the UV absorbance of the resulting solution against a standard curve. Encapsulation efficiencies (EE) were calculated using the following formula:

$$EE = \frac{C_e}{C_i} \times 100\%$$

Photodynamic properties

***In vitro* ROS detection.** The ROS generation was measured based on the reported method.[29] DCF-DA was used as an indicator since the emission of DCF-DA increases upon reacting with ROS. Initially, 0.1 mL of 1 mM DCF-DA in DMSO was added to 1 mL of 0.01 M NaOH, and the resulting solution was stirred for 30 minutes at room temperature. The mixture was then neutralized with 19 mL of PBS (pH 7.4). The hydrolysis product, dichlorofluorescein (5 μM), was mixed with 10 μM TTO or TTS in THF/water (10 : 90, v/v) and exposed to 635 nm red laser light irradiation (200 mW cm^{-2}). The oxidized DCF was monitored by recording the emission increment at 525 nm. The ROS generation capability of methylene blue was also evaluated as a control. The data were subsequently organized and presented in charts.

***In vitro* ^{1}O$_2$ sensitization evaluation.** Scavenger assays were performed to support singlet oxygen sensitization, wherein the

ROS generation capability of TTO and TTS was assessed following the identical method as extracellular ROS detection, but with the addition of a 10 μM singlet oxygen-specific scavenger, tris(4-bromophenyl)amine (TBPA). The data were subsequently organized and presented in charts.

Cell culture

LM8 cells and SMCs were obtained from the American Type Culture Collection (ATCC). The cells were maintained at 37 °C in a humidified incubator with 5% CO_2, cultured in DMEM medium supplemented with 10% fetal bovine serum (FBS) and 1% penicillin-streptomycin. Routine mycoplasma testing confirmed the absence of contamination.

Cytotoxicity study

SMCs with good growth status were cultured in a 5% CO_2 atmosphere at 37 °C until confluent monolayers formed in 96-well flat-bottom plates. Ten randomly selected wells were evenly divided into two groups and co-incubated with TTO NPs/TTS NPs at varying concentrations (10–50 μmol L^{-1}, calculated based on fluorophore standards) for 24 hours under light irradiation or in the dark. After incubation, 20 μL of 3-(4,5-dimethylthiazol-2-yl)-2,5-diphenyltetrazolium bromide (MTT) solution (5 mg mL^{-1}) was added to each well, followed by an additional 4 hours of incubation. The culture medium was then aspirated, and 100 μL of DMSO was added to dissolve formazan crystals. Plates were shaken at low speed for 10 min on an orbital shaker, and absorbance at 490 nm was measured using a microplate reader. Results were compiled into a bar graph for comparative analysis.

In vivo imaging

The C3H mice were purchased from Beijing Vitalstar Biotechnology Co., Ltd. All animal studies were conducted under the guidelines set by Tianjin Committee of Use and Care of Laboratory Animals, and the overall project protocols were approved by the Animal Ethics Committee of Nankai University. Following hair removal treatment on the right axilla, the mice were respectively injected with 50 μL of LM8 cell suspension (1 × 10^7 cells). After 15 days, when the tumor diameter reached approximately 100 mm, fluorescence imaging and biodistribution experiments were initiated. TTO and TTS NPs solid powders were weighed and dissolved in PBS buffer to prepare a stock solution. A 160 μmol L^{-1} solution of TTO NPs/TTS NPs was prepared. Two C3H mice with LM8 subcutaneous tumors were administered 100 μL of the prepared TTO NPs and TTS NPs solutions (160 μmol L^{-1}) respectively via tail vein injection. Twenty-four hours post-injection for TTO NPs and TTS NPs, the mice were anesthetized with isoflurane and scanned using a small animal NIR imaging system (IVIS Lumina II) for fluorescence imaging. During imaging, the mice were continuously anesthetized with 3% isoflurane delivered through a nose cone. Based on fluorescence imaging, the subcutaneous tumors were excised, and the mice were euthanized by cervical dislocation. The heart, liver, spleen, lungs, and kidneys were collected, washed, and imaged using the IVIS Lumina II system to obtain fluorescence and bioluminescence images.

Abbreviations

FGS	Fluorescence-guided surgery
NIR	Near-infrared
TBA	Thiobarbituric acid
ICT	Intramolecular charge transfer
AIE	Aggregation-induced emission
ROS	Reactive oxygen species
NPs	Nanoparticles
EPR	Enhanced permeability and retention
OS	Osteosarcoma
ACQ	Aggregation-caused quenching
TPE	Tetraphenylethylene
Tol	Toluene
DCM	Dichloromethane
THF	Tetrahydrofuran
DMSO	Dimethyl sulfoxide
TICT	Twisted intramolecular charge transfer
PDT	Photodynamic therapy
DCF-DA	2′,7′-Dichlorodihydrofluorescein diacetate
DCF	2′,7′-Dichlorofluorescein
DFT	Density functional theory
TD-DFT	Time-dependent density functional theory
HOMO	Highest occupied molecular orbital
LUMO	Lowest unoccupied molecular orbital
ISC	Intersystem crossing
DLS	Dynamic light scattering
MTT	3-(4,5-Dimethylthiazol-2-yl)-2,5-diphenyltetrazolium bromide
SMCs	Smooth muscle cells
TEM	Transmission electron microscopy

Data availability

The data supporting this article have been included as part of the ESI.†

Conflicts of interest

There are no conflicts to declare in this article.

Notes and references

1 A. Misaghi, A. Goldin, M. Awad and A. A. Kulidjian, *Scot. J.*, 2018, **4**, 12.

2 X. Zhao, Q. Wu, X. Gong, J. Liu and Y. Ma, *Biomed. Eng. Online*, 2021, **20**, 24.

3 F. Jafari, S. Javdansirat, S. Sanaie, A. Naseri, A. Shamekh, D. Rostamzadeh and S. Dolati, *Ann. Diagn. Pathol.*, 2020, **49**, 151654.

4 R. A. Durfee, M. Mohammed and H. H. Luu, *Rheumatol. Ther.*, 2016, **3**, 221–243.

5 L. J. Lauwerends, P. B. A. A. van Driel, R. J. Baatenburg de Jong, J. A. U. Hardillo, S. Koljenovic, G. Puppels, L. Mezzanotte, C. W. G. M. Löwik, E. L. Rosenthal, A. L. Vahrmeijer and S. Keereweer, *Lancet Oncol.*, 2021, **22**, e186–e195.

6 J. S. D. Mieog, F. B. Achterberg, A. Zlitni, M. Hutteman, J. Burggraaf, R.-J. Swijnenburg, S. Gioux and A. L. Vahrmeijer, *Nat. Rev. Clin. Oncol.*, 2021, **19**, 9–22.

7 R. M. Schols, N. J. Connell and L. P. S. Stassen, *World J.Surg.*, 2014, **39**, 1069–1079.

8 P. A. Sutton, M. A. van Dam, R. A. Cahill, S. Mieog, K. Polom, A. L. Vahrmeijer and J. van der Vorst, *BJS Open*, 2023, **7**, 3.

9 L. G. Wang and S. L. Gibbs, *Curr. Opin. Chem. Biol.*, 2023, **76**, 102361.

10 Y. Hong, J. W. Y. Lam and B. Z. Tang, *Chem. Commun.*, 2009, **29**, 4332–4353.

11 Y. Hong, J. W. Y. Lam and B. Z. Tang, *Chem. Soc. Rev.*, 2011, **40**, 5361–5388.

12 K. Ren, B. Zhang, J. Guo, H. Cao, J. Cheng, J. Guo and D. Li, *Biosens. Bioelectron.*, 2025, **271**, 117067.

13 Q. Xia, Y. Zhang, Y. Li, Y. Li, Y. Li, Z. Feng, X. Fan, J. Qian and H. Lin, *Aggregate*, 2022, **3**, e152.

14 J. Dai, H. Xue, D. Chen, X. Lou, F. Xia and S. Wang, *Coord. Chem. Rev.*, 2022, **464**, 214552.

15 W. He, Z. Zhang, Y. Luo, R. T. K. Kwok, Z. Zhao and B. Z. Tang, *Biomaterials*, 2022, **288**.

16 J. Qian and B. Z. Tang, *Chem*, 2017, **3**, 56–91.

17 H. Wang, Q. Li, P. Alam, H. Bai, V. Bhalla, M. R. Bryce, M. Cao, C. Chen, S. Chen, X. Chen, Y. Chen, Z. Chen, D. Dang, D. Ding, S. Ding, Y. Duo, M. Gao, W. He, X. He, X. Hong, Y. Hong, J.-J. Hu, R. Hu, X. Huang, T. D. James, X. Jiang, G.-i. Konishi, R. T. K. Kwok, J. W. Y. Lam, C. Li, H. Li, K. Li, N. Li, W.-J. Li, Y. Li, X.-J. Liang, Y. Liang, B. Liu, G. Liu, X. Liu, X. Lou, X.-Y. Lou, L. Luo, P. R. McGonigal, Z.-W. Mao, G. Niu, T. C. Owyong, A. Pucci, J. Qian, A. Qin, Z. Qiu, A. L. Rogach, B. Situ, K. Tanaka, Y. Tang, B. Wang, D. Wang, J. Wang, W. Wang, W.-X. Wang, W.-J. Wang, X. Wang, Y.-F. Wang, S. Wu, Y. Wu, Y. Xiong, R. Xu, C. Yan, S. Yan, H.-B. Yang, L.-L. Yang, M. Yang, Y.-W. Yang, J. Yoon, S.-Q. Zang, J. Zhang, P. Zhang, T. Zhang, X. Zhang, X. Zhang, N. Zhao, Z. Zhao, J. Zheng, L. Zheng, Z. Zheng, M.-Q. Zhu, W.-H. Zhu, H. Zou and B. Z. Tang, *ACS Nano*, 2023, **17**, 14347–14405.

18 D. Chen, T. Xiao, L. Wang, S. Chen, C. Kam, G. Zeng, L. Peng, J. Zhang, M. Li and Y. Dong, *Aggregate*, 2024, **5**, e550.

19 Z. Xiong, W. Gong, P. Xu, M. Jiang, X. Cai, Y. Zhu, X. Ping, H. Feng, H. Ma and Z. Qian, *Chem. Eng. J.*, 2023, **451**, 139030.

20 J. H. Correia, J. A. Rodrigues, S. Pimenta, T. Dong and Z. Yang, *Pharmaceutics*, 2021, **13**, 1332.

21 M. Overchuk, R. A. Weersink, B. C. Wilson and G. Zheng, *ACS Nano*, 2023, **17**, 7979–8003.

22 Z. Jiang, B. Wen, Y. Huang, Y. Wang, H. Fang and F. Li, *J. Am. Chem. Soc.*, 2025, **147**, 10992–10998.

23 C. Chen, Z. Song, X. Zheng, Z. He, B. Liu, X. Huang, D. Kong, D. Ding and B. Z. Tang, *Chem. Sci.*, 2017, **8**, 2191–2198.

24 H. Nie, K. Hu, Y. Cai, Q. Peng, Z. Zhao, R. Hu, J. Chen, S.-J. Su, A. Qin and B. Z. Tang, *Mater. Chem. Front.*, 2017, **1**, 1125–1129.

25 T. Hua, L. Zhan, N. Li, Z. Huang, X. Cao, Z. Xiao, S. Gong, C. Zhou, C. Zhong and C. Yang, *Chem. Eng. J.*, 2021, **426**, 131169.

26 D. Zhong, D. Jia, X. Yang, Y. Sun and G. Zhou, *Org. Electron.*, 2023, **113**, 106706.

27 J. Liu, M. Evrard, X. Cai, G. Feng, N. Tomczak, L. G. Ng and B. Liu, *J. Mater. Chem. B*, 2018, **6**, 2630–2636.

28 A. Rananaware, R. S. Bhosale, K. Ohkubo, H. Patil, L. A. Jones, S. L. Jackson, S. Fukuzumi, S. V. Bhosale and S. V. Bhosale, *J. Org. Chem.*, 2015, **80**, 3832–3840.

29 Y. Li, J. Zhuang, Y. Lu, N. Li, M. Gu, J. Xia, N. Zhao and B. Z. Tang, *ACS Nano*, 2021, **15**, 20453–20465.